

Chapter 4

Western Disturbances – Indian Winter Monsoon

Abstract In this chapter, wintertime dynamics associated with large-scale flow and western disturbances (WDs) influencing winter precipitation is proposed and termed ‘Indian winter monsoon’. In Indian meteorological research, the northeast monsoon and Indian winter monsoon terms are interchangeable. In addition, winter precipitation – the Indian winter monsoon – is assumed to be similar to an extra-tropical cyclone traveling in large-scale westerlies. With concurrent research and the changing global context, increased understanding of the Indian winter monsoon is imperative. This chapter delineates the Indian winter monsoon while differentiating it from the northeast monsoon which so far is the prevalent term used in Indian meteorological parlance. Therefore, the present chapter provides comprehensive details on defining the Indian winter monsoon.

The Indian subcontinent is characterized by unique geographic positioning. The north is surrounded by the mighty Himalayas and the south by ocean. Such situations, along with many the seasonal changes, give rise to different weather patterns over the Indian subcontinent. The Indian summer monsoon (June, July, and August – JJA) (ISM) has been studied and discussed along with its varying dimensions (Annamalai et al. 2007; KrishnaKumar et al. 1999, 2006; Turner et al. 2007; Saha et al. 2011) such as the Tibetan high, which also well plays a significant role in defining the strength of ISM (Yasunari et al. 1991; Wu and Qian 2003; Sato and Kimura 2007). In the case of the northeast monsoon (NEM), Kripalani and Kumar (2004), Kumar et al. (2007) and Yadav (2012) have deliberated upon its dynamics comprehensively. On another regional scale, non-monsoon periods as well are of great importance for the Indian region. In winter (December, January, and February–DJF), accumulation in the form of snow provides important feed to the north Indian rivers, glacier etc. (Dai 1990; Lang and Barros 2004; Yadav et al. 2013; Dimri 2014). This precipitation is mainly contributed by the extra-tropical cyclones called WDs (Dimri and Mohanty 2009; Dimri et al. 2013). Though there are various studies available on the ISM and NEM, very limited information is available on the Indian winter monsoon (IWM) (Dimri 2004, 2006, 2012, 2013a; Yadav et al. 2013). Only very few studies have focused on the IWM variability (Laat and Lelieveld 2002; Dimri 2012, 2013a, b, 2014; Yadav et al. 2013).

4.1 Introduction

Many studies have defined dominant intraseasonal (ISO) modes that vary at different time scales for ISM (Hartmann and Michelsen 1989; Goswami and Mohan 2001; Hoyos and Webster 2007). Though the interannual variations (IAVs) in the IWM are in phase with ENSO forcings (Yadav et al. 2010; Dimri 2012, 2013a), much less has been explained concerning its ISOs behavior (Dimri 2014). Since most of the Indian economy and agriculture is driven by ISM and derived from to its broader impact, most of the research is focused on understanding and defining the ISM. Apart from the contribution to winter precipitation over the northern Indian region, interaction of IWM with the northern Indian Himalayas topography and land use, paucity of observations, solid – liquid precipitation ratio and snow-covered land-surface interactions are research questions that still need to be debated. With concurrent research and the changing global context, the impacts of sub-continental-scale circulation changes during the IWM over northern India are imperative. In order to define the IWM, this chapter elaborates on the potential role of sub-continental and global-scale circulation changes and interannual and intraseasonal behavior associated with the IWM. Such deliberation will provide new dimensions and definition to the understanding of IWM in Indian meteorological parlance which has been missing thus far. The following sections sequentially deliberate upon the important dynamics associated with the IWM.

To understand the winter precipitation over the northern Indian region dataset in this chapter, these sources are used: Asian Precipitation – Highly-Resolved Observational Data Integration Towards Evaluation of Water Resources (APHRODITE, Yatagai et al. 2012), Global Precipitation Climatology Project (GPCP, Adler et al. 2003), Global Precipitation Climatology Centre (GPCC, Rudolf et al. 2005) and Climate Research Unit (CRU, New et al. 2000). Corresponding winter precipitation over the western Himalayas (WH) is shown in Fig. 4.1a. The reason for using multiple sets of precipitation data is to assess the spatial variability in different precipitation fields over the WH region. It is important because this region has a paucity of observations and possesses land-use heterogeneity and topographic variability. Wind, moisture and geopotential fields are taken from the National Center of Environmental Prediction/National Center for Atmospheric Research (NCEP/NCAR) (Kanamitsu et al. 2002). Sea-surface temperature (SST) is incorporated from the Hadley Center, UK (Hadley Center 2006). Outgoing long-wave radiation (OLR) from the National Oceanic and Atmospheric Administration (NOAA) in the US (Liebmann and Smith 1996) is also used to identify such seasonal and ground dependency. Data from 28 winters (1979–2007) for geopotential height, wind, stream function, moisture flux etc. are considered to examine ISOs associated with the IWM.

Most of the algorithms used in preparing precipitation reanalyses generate ‘synthetic’ precipitation values which sometimes deviate from the real observations. To remove this ‘probable’ bias of inadequate representation, a mask field of a 10 mm/month precipitation threshold is used. Also, precipitation, OLR, and reanalysis of

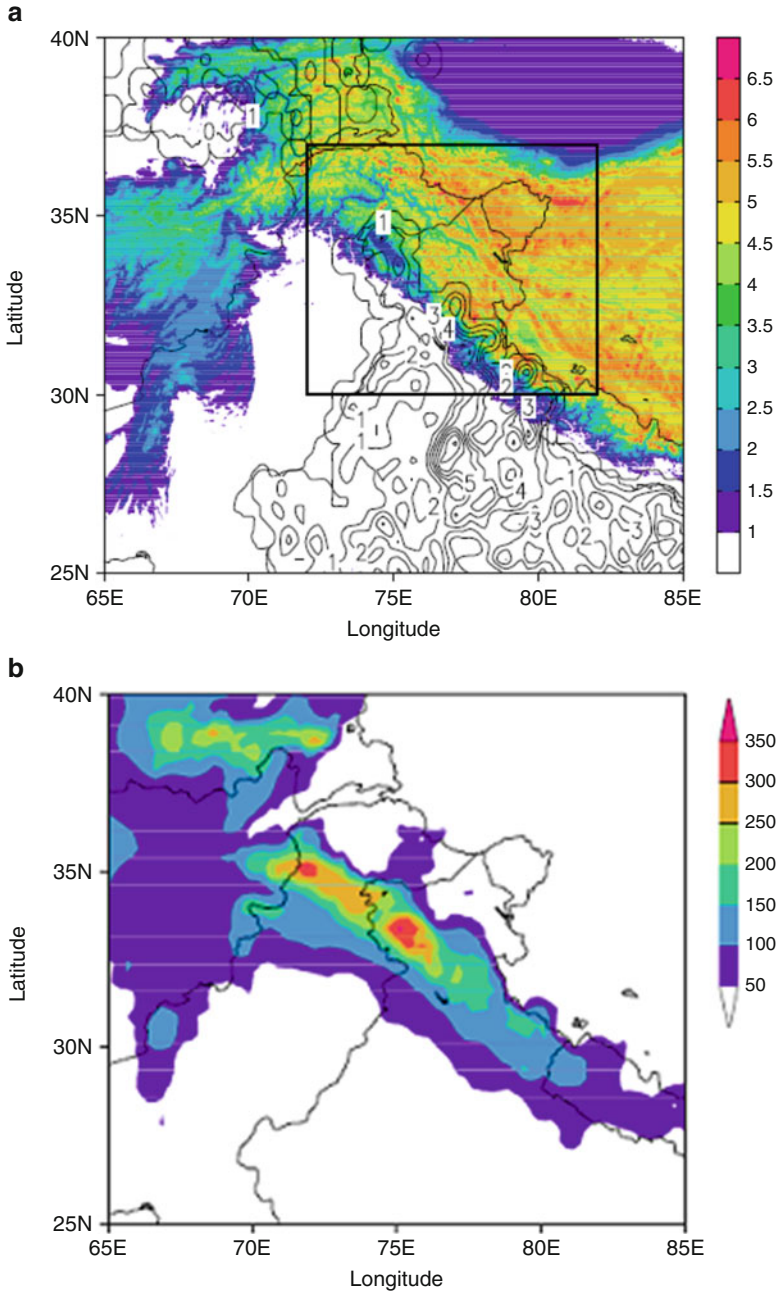


Fig. 4.1 (a) Topography ($\times 1e-3$ m; *shaded*) and ratio of 0.05° grids for stations (%; *contour*) over the western Himalayas. The area of 30°N , 72°E to 37°N , 82°E is considered in the present chapter; (b) winter season precipitation climatology (mm/DJF) based on APHRODITE precipitation observed data reanalysis

daily data anomalies are homogenized and deseasonalized. For each year, the first three harmonics of the annual cycle (about 120 days) are subtracted from the anomaly time series to homogenize it. Then to deseasonalize/detrend the time series, sub-monthly (7–25 days) perturbations were computed by applying a Lanczos filter (Duchon 1979). In the WH, the region from 30°N 72°E to 37°N 82°E (indicated by the box in Fig. 4.1a) was chosen to analyse winter precipitation and associated IAV and ISO. This region was chosen because the area receives the highest winter precipitation and is topographically variable. Figure 4.1b shows the seasonal precipitation climatology based on reanalysis of APHRODITE observations. Winter precipitation climatology is distributed across and along the WH topographic orientation. Precipitation maxima at ~34°N 76°E and ~35°N 72°E are observed. This climatology was compared with the other reanalysis data (GPCP, GPCC, and CRU). Correlations of greater than 0.8 were recorded between APHRODITE data and these reanalysed data. Over the WH, spatial precipitation patterns of precipitation in all four gridded precipitation reanalyzes are similar. Of these four reanalyzes, APHRODITE reanalysis is used for further analysis and discussion because they have the finest spatial resolution. It should be noted that over such a region, some data may be ‘synthetic’ due to the various algorithms used while preparing the reanalysis of precipitation fields. However, this issue is beyond the scope of the present chapter.

4.2 Interannual Variability of the Indian Winter Monsoon

A physical mechanism of the IWM over the WH with reference to excess/deficit years and their year-to-year variability is discussed based on the period 1980–2007 (28 years). In the following paragraphs, explanations with specific reference to the sub-continental and global-scale circulation changes are provided followed by deliberations on the role of the sea-surface warming/cooling phase and associated circulation patterns in defining winter precipitation over the WH.

Interannual variability associated with IWM over the WH is explained with composite sets of wet and dry years with the study area shown in Fig. 4.1. Based on ± 0.5 standard deviation, wet (1983, 91, 92, 95, 98, 2005) and dry (1985, 88, 97, 2000, 01, 06) precipitation years are chosen. The region from 30°N 72°E to 37°N 82°E (marked by the box in Fig. 4.1a) is selected as it receives the highest winter precipitation. Seasonal and monthly area-averaged winter precipitation anomaly is shown in Fig. 4.2a. There are years having excess and deficit precipitation over the region. Corresponding wet-dry composite precipitation differences, with 99 % confidence, are depicted in Fig. 4.2b. It shows that the significant region of higher precipitation is oriented along the WH topography which corroborates with Dimri and Niyogi (2012). On global-scale circulation patterns, 200 hPa zonal wind differences between wet and dry year composites show southward movement of the SWJ over and across the Indian subcontinent (Fig. 4.3a). In the mid-latitude region, steep pressure-gradient anomalies attribute to these stronger westerlies (Raman and

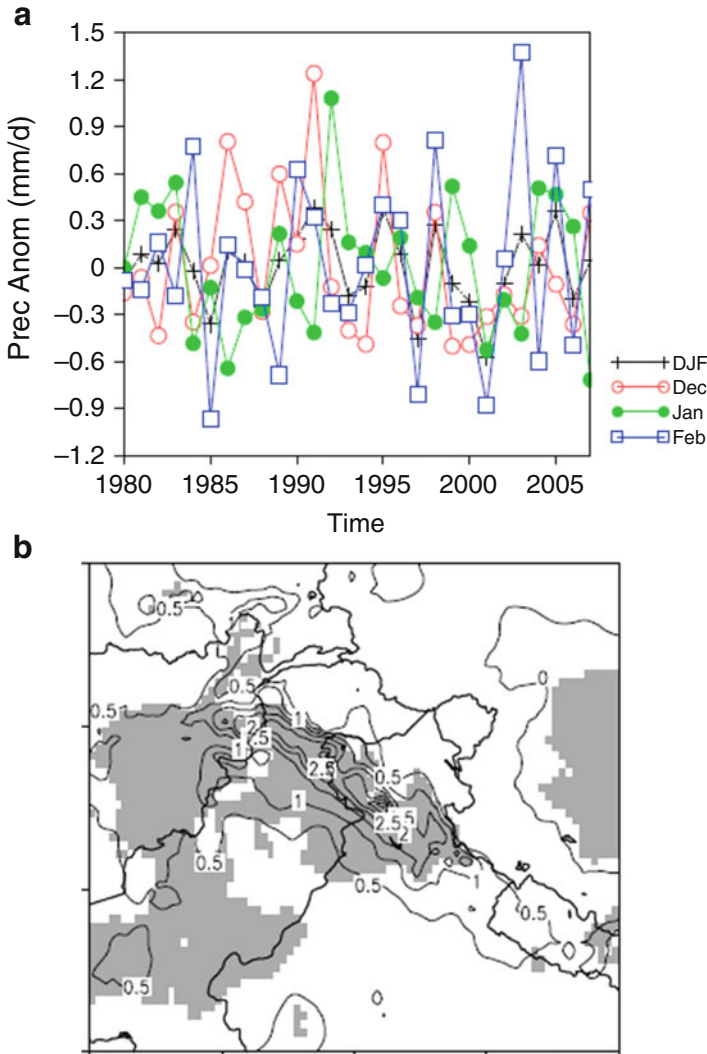


Fig. 4.2 (a) The monthly (Dec, Jan, and Feb) and seasonal (DJF) precipitation (mm/d) anomaly in APHRODITE observational reanalysis and (b) difference in 3-month (Dec, Jan, and Feb) average wet- and dry-year composites precipitation (*shaded*) and region with 99 % confidence level (*within contour*)

Maliekal 1985). At 500 hPa (Fig. 4.3b), significant lower geopotential is visible right from Saudi Arabia to the head of the Arabian Sea extending along 10°N to 30°N. Weaker westerlies dominate from the Black Sea region to the northwest Indian and Tibetan Plateau region in and around 30°N. During wet years, at lower level (850 hPa – Fig. 4.3c) over the head of the Arabian Sea, a weak anomalous cyclonic surface low persists. Such mid-tropospheric circulations provide necessary

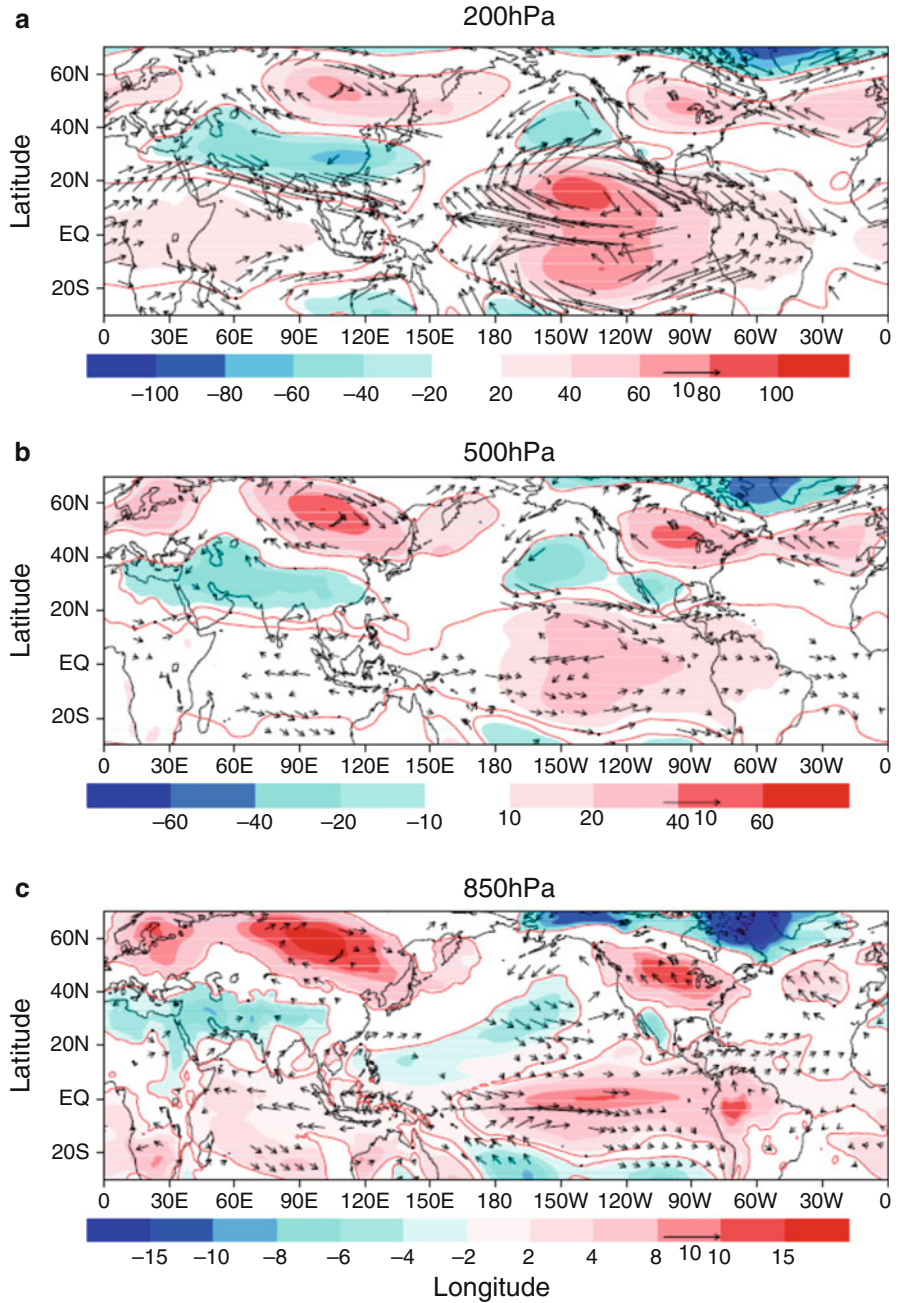


Fig. 4.3 Difference between 03 (DJF) month average wet and dry composites of wind (m/s; contour; winds above 99 % significant level are plotted) and geopotential height (m; shaded; region within contour corresponds to 99 % significant level) at (a) 200 hPa (b) 500 hPa and (c) 850 hPa

convergence augmenting the precipitation mechanism by enhancing moisture supplement from the Caspian and Arabian Seas. Further, an axis of anomalous anticyclone dominates along $\sim 60^{\circ}\text{N}$ 120°E at 200 hPa exists (see Fig. 4.3a). Another anomalous anticyclone extends from the central African continent to the Indian Ocean and up to Indonesia. A strong anomalous cyclone separates these two anomalous anticyclones and overruns the Indian subcontinent. In wet years, due to such enhanced anomalous highs and lows, the SWJ shifts southwards. The upper-level circulation patterns persist down into the mid-troposphere as well during the wet winters (Fig. 4.3b). Such stronger meridional pressure gradients provide favorable conditions for frontal WDs formations. During winter, these characteristic fronts in mid-latitude westerlies generate troughs in a sequential manner, and this is responsible for the genesis of a number of WDs. In wet years, at 850 hPa, stronger anomalous cyclonic circulation at and around $\sim 18^{\circ}\text{N}$ 62°E dominates (Fig. 4.3c). Slower westerlies around the equator and a deepening of northwesterlies over the Arabian Sea exist during wet years. Such deepening brings in moisture flux over the WH during the wet years. In addition, vertical distributions of cyclonic formations immediately west of the WH create favorable conditions for higher precipitation. Anomalous velocity potential and corresponding OLR at upper troposphere are presented in Fig. 4.4a and b for wet and dry year composites, respectively. In wet times, significant strong inflow (outflow) over the equatorial western (eastern) Pacific dominates (Fig. 4.4a). In dry year composites, a weak convergent source over the equatorial central Pacific is apparent (Fig. 4.4b). In addition, during wet years, the equatorial central (western) Pacific is associated with increased (decreased) convective activity. Further, lower-level increased (decreased) convection over the equatorial eastern (western) Pacific is associated with strong upward (downward) motion. In boreal winter, such situations attribute to enhanced north-south circulation in the upper tropospheric branch of the zonally-symmetric Hadley circulation. Corresponding OLR distributions show strong (weak) convection followed by pronounced (reduced) cloud formation and hence reduced (enhanced) OLR over the equatorial central (western) Pacific region (Fig. 4.4a). A slightly decreased OLR over the WH and western Indian Ocean, which also corresponds to increased cloud formation, is also observed. The upper-tropospheric anomalous stream function (representing rotational part of wind) with the corresponding anomalous OLR is depicted for wet and dry year composites (Fig. 4.4c, d respectively). A well-defined anomalous cyclonic core is seen over the WH. In addition, an upper-tropospheric low/cyclonic circulation dominates from the Mediterranean Sea to the western Pacific. ElNiño formed enhanced cooling over the western equatorial tropical Pacific and hence the corresponding Rossby responses (Kawamura 1998) creates cyclonic formulations over the WH. In this dry situation, anticyclonic/divergent circulation dominates over the WH (Fig. 4.4d.)

The antecedent dependency of the IWM is investigated here. The lagged correlation between winter precipitation over the WH and sea-surface temperatures for 28 years (1980–2007) is presented in Fig. 4.5. The IWM shows persistent and strong correlation with equatorial warming in previous seasons. Significant strong (negative) positive correlation with the eastern (western) equatorial Pacific warming

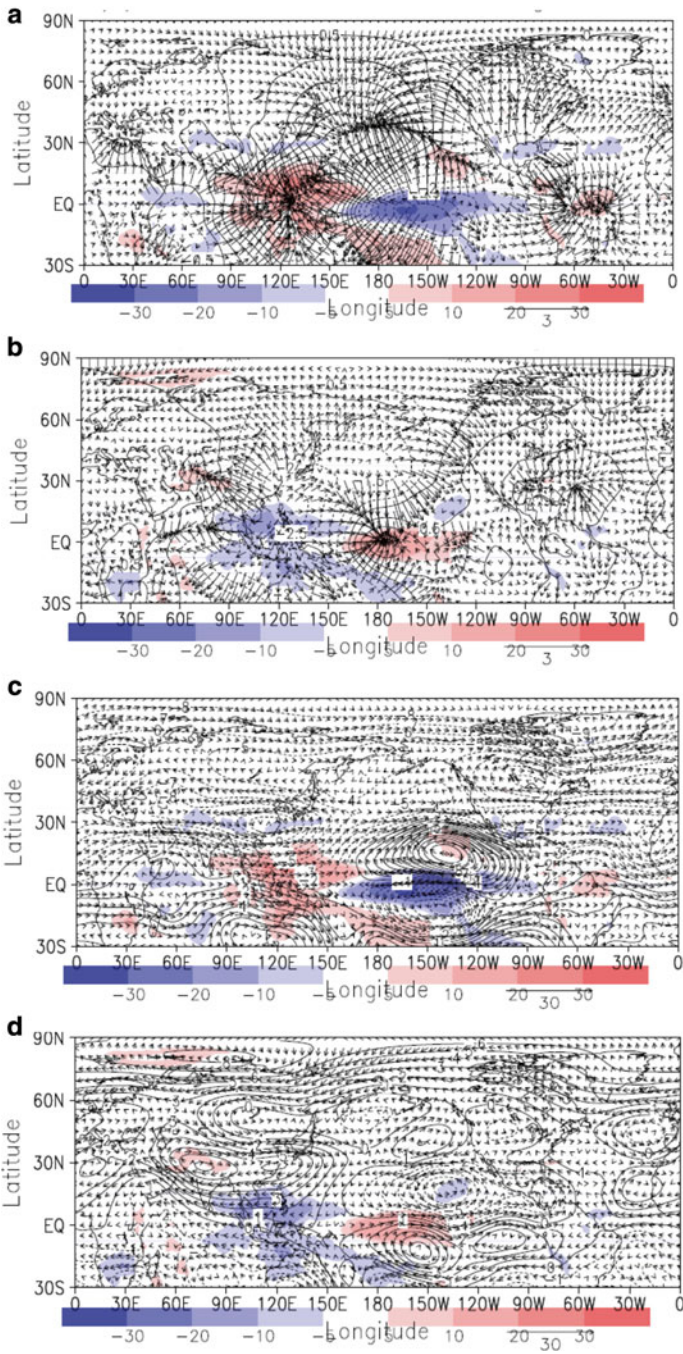
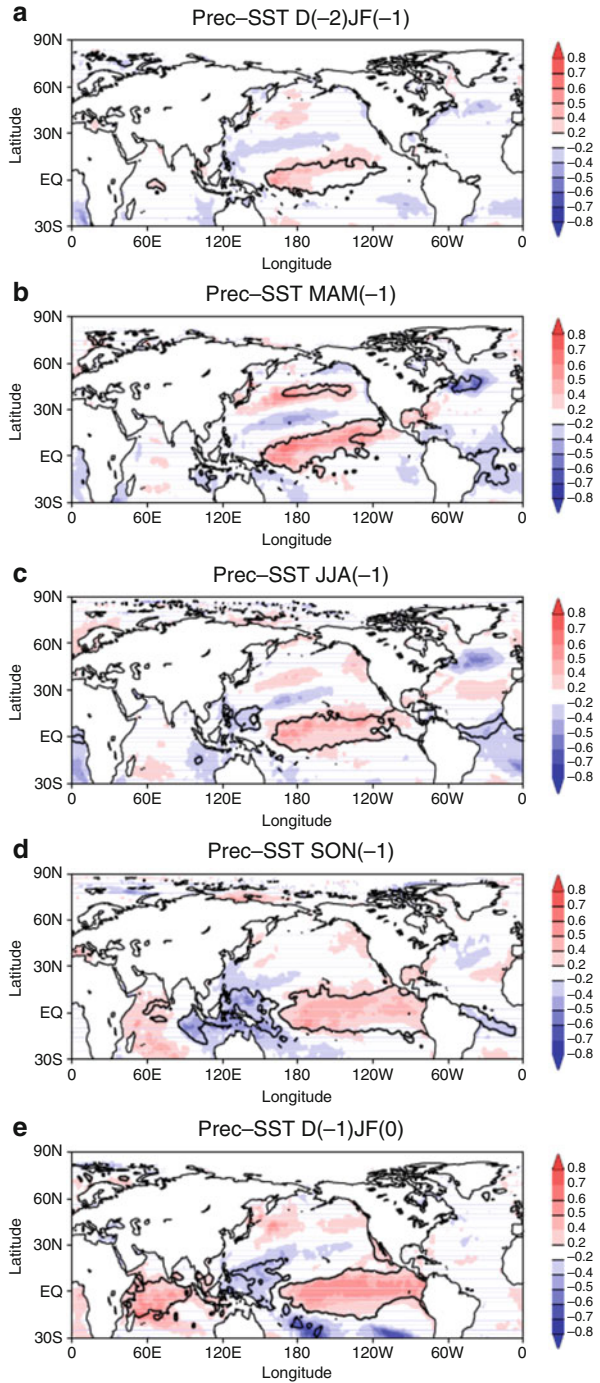


Fig. 4.4 Seasonal anomalous velocity potential ($\times 10^{-6} \text{ m}^2/\text{s}$; contour) with corresponding anomalous divergent wind (m/s ; arrow) at $\sigma=0.1682$ and anomalous outgoing longwave radiation (W/m^2 ; shade) for (a) wet and (b) dry year composites and seasonal anomalous stream function ($\times 10^{-6} \text{ m}^2/\text{s}$; contour) with corresponding anomalous rotational wind (m/s ; arrow) at $\sigma=0.1682$ and anomalous outgoing longwave radiation (W/m^2 ; shade) for (c) wet and (d) dry year composites

Fig. 4.5 Correlation between 28 years (1980–2007) area averaged winter precipitation $-D(-1)$ JF(0) – (mm/d) with sea surface temperature ($^{\circ}$ C) during (a) D(-2)JF(-1) (b) MAM(-1) (c) JJA(-1) (d) SON(-1) and (e) D(-1) JF(0). (Figures in bracket correspond to sea surface temperature with previous and corresponding seasons). Region within contour corresponds to 99 % significant level

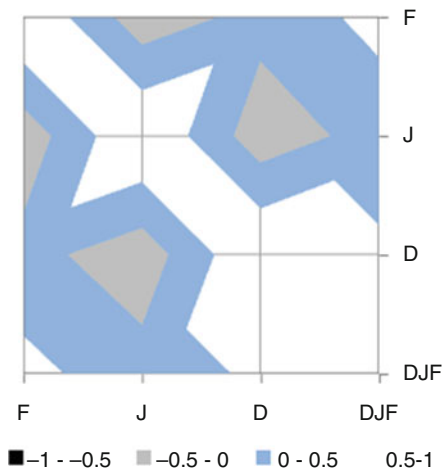


(cooling) is seen already by the previous winter (concurrent summer) season (Fig. 4.5a–e). This significant positive correlation with Indian Ocean warming increases (Fig. 4.5d, e) corresponds to the buildup of the IWM by the previous season (September, October, and November). By winter, equatorial eastern (western) Pacific warming (cooling) with the equatorial Indian-Ocean warming corroborate to create a stronger IWM. Warming over the Indian Ocean enhances the northward gradient for mass transfer and hence increased response of the Hadley cell. This robustness, in tandem with functioning of the enhanced Hadley cell and the attenuated Walker circulation, corresponds to the strengthened increased IWM, which previously was not well known (Oort and Yienger 1996; Mitras and Clement 2005).

4.3 Sub-seasonal Oscillation Associated with the Indian Winter Monsoon

As discussed in the preceding section, monthly (December, January, and February) interannual variabilities in precipitation are positively correlated with the corresponding seasonal (DJF) interannual variability in precipitation, but they are not in phase with each other. January interannual variability is negatively correlated with December and February interannual variabilities (Fig. 4.6). Seasonal (DJF) interannual precipitation variability is positively correlated with individual monthly interannual precipitation variability (0.60 for December, 0.20 for January, and 0.65 for February: Fig. 4.6). December and February show a higher degree of correlation than does January. It was found, however, that monthly anomalous interannual variabilities in the winter months (December, January, and February) were negatively correlated with one another. January interannual variability was negatively correlated with interannual variability in December (−0.29) and February (−0.30). ENSO

Fig. 4.6 Correlation between seasonal (DJF) and monthly (Dec, Jan, and Feb) interannual precipitation variability based on APHRODITE



forcing has a similar behavior during the whole season (DJF), and thus the reason that the January interannual variability is opposite to that of December and February is unclear. To address this question, a seasonal and monthly composite analysis for selected extreme precipitation years is performed to explain it further during the IWM. In the following paragraphs, discussion of the linkages of the IWM with global and local forcings to determine the reasons for the contrasting behavior of monthly interannual variabilities is presented.

4.3.1 Wet and Dry Winters over the WH and Its Associated Circulation

Initially, the corresponding composite monthly anomalous precipitation distribution during wet (Fig. 4.7a, b, and c) and dry (Fig. 4.7d, e, and f) years was analyzed. To remove the effect of inadequate in situ observations from the observational reanalysis, field masking with a 10 mm/month threshold was employed. The result indicates that January anomalous precipitation is reduced (enhanced) more during wet (dry) years (see Fig. 4.7b, e) than in December (Fig. 4.7a, d), and February (Fig. 4.7c, f). The January composite precipitation for wet (dry) years shows less (more) precipitation than the December and February values. In the case of composite precipitation for dry years, January shows a relatively higher anomalous precipitation when compared with December and February. Such contrasting sub-seasonal behavior during IWM is presented, deliberated and a rationale for such patterns and associated variability is developed.

During extreme winter, significant anomalous cyclonic circulation associated with the IWM exists over the Himalayas due to suppressed convection over the western equatorial tropical Pacific (Kawamura 1998; Dimri 2012, 2013a). To assess this dynamical role during the excess and deficit IWM, Fig. 4.8 presents wet-minus-dry composites at the 200 hPa height (contours) and wind (vector) for December (Fig. 4.8a), January (Fig. 4.8b), and February (Fig. 4.8c), respectively. The hatched region corresponds to a $\geq 95\%$ significance level. Similarly, only wind data at the $\geq 95\%$ significance level is shown. Broad differences between the wet and dry monthly composites indicate that, in the upper troposphere, a significant anomalous cyclonic circulation extending up to the South China Sea prevails over the Himalayas during December and February, which weakens during January and is not significant. Another anomalous anticyclonic circulation located over the Siberian region during December weakens and becomes more elongated during January and shifts northward during February. During January, a well-defined anomalous anticyclonic circulation exists over the North African region to the west of the Himalayas. Corresponding wind fields suggest that, over the north Himalayas/Tibetan Plateau, slower westerlies prevail during wet years. In particular, slower westerlies dominate during December and February. In the mid-troposphere, at 500 hPa, anomalous cyclonic circulation over and around the WH prevails during December and January

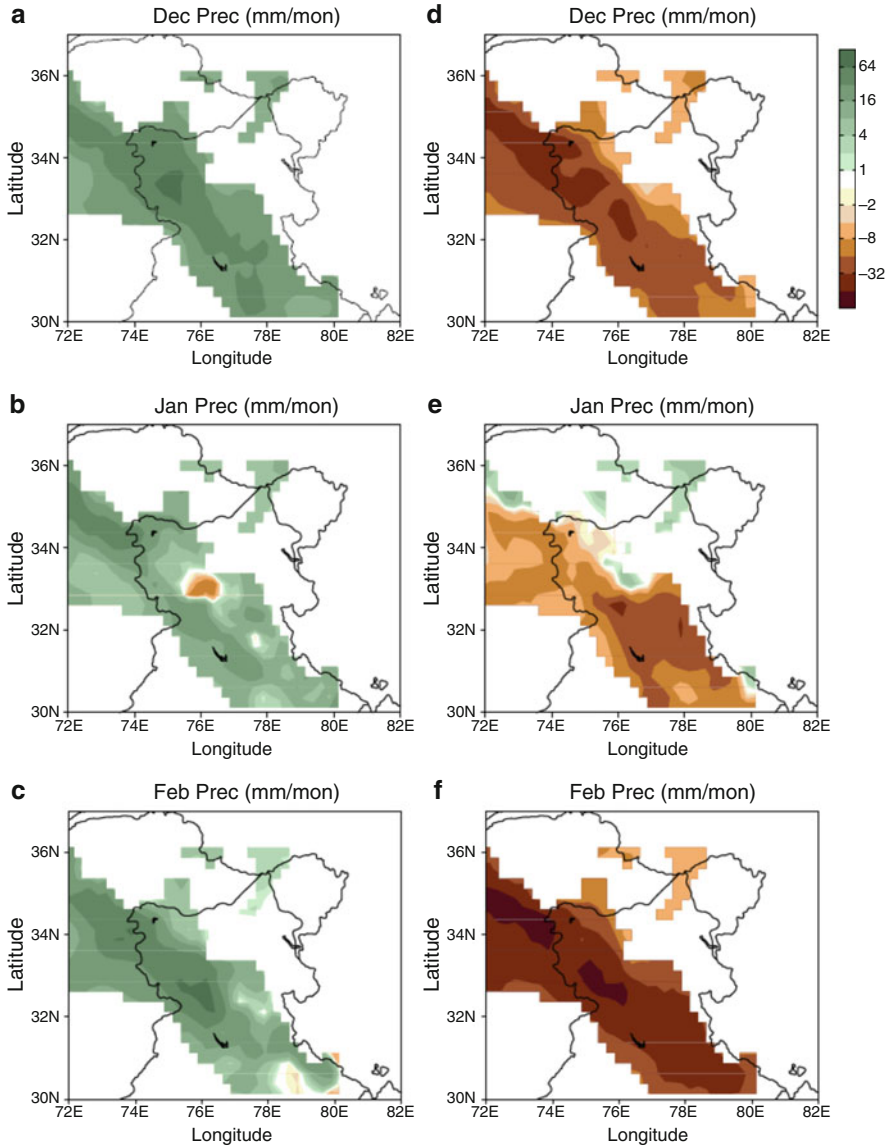


Fig. 4.7 Cumulative average monthly anomalous precipitation (mm/month) during wet composites of (a) Dec, (b) Jan, and (c) Feb and for dry composites of (d) Dec, (e) Jan, and (f) Feb. Masking with 10 mm/month was employed

(data not shown). Detailed scrutiny indicates that, during December, an elongated significant anomalous cyclonic circulation spreads over the west of the Himalayan region and then decays during January. However, an anomalous anticyclonic circulation over the Caspian Sea region prevails, which strengthens during January and

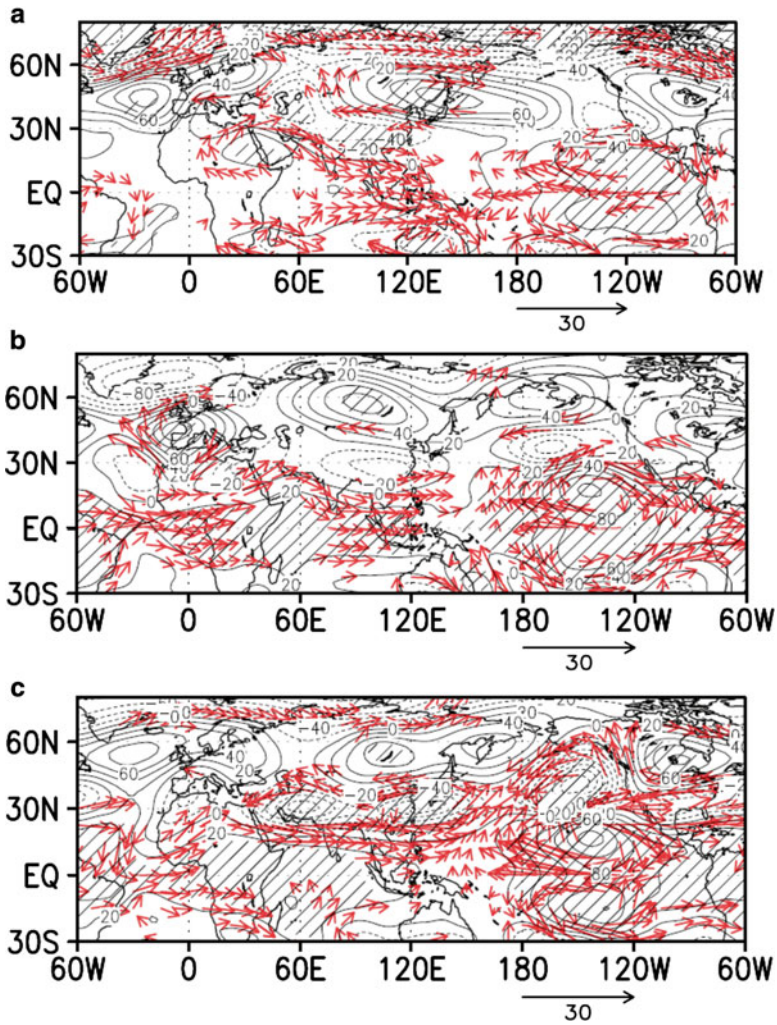


Fig. 4.8 Monthly difference in (wet–dry) anomaly for 200 hPa geopotential height (hPa, *contour*) and wind vector (ms^{-1} , *arrow*) for (a) Dec, (b) Jan, and (c) Feb. The hatched region corresponds to $\geq 95\%$. Similarly, only winds with 95% significance and above are shown

becomes an anomalous cyclonic circulation during February. It was observed that during January, the anomalous cyclonic circulation weakens over the Himalayas, in contrast to the situation observed during December and February. Corresponding significant wind data indicates that winds over the equatorial Indian Ocean, which are slower westerlies during December, are almost neutral during January and then become faster during February. In addition, northward propagation weakens during January. In the lower troposphere, at 850 hPa, stronger northwest wind propagation dominates during December and February, becoming almost neutral during January

(data not shown). This propagation at the surface, arising from moisture-flux transport from the equatorial Indian Ocean to the WH, strengthens the IWM during December and February more than during January.

Corresponding air-temperature conditions associated with the IWM illustrates the upper tropospheric wet-minus-dry composite air temperature distribution (data not shown). It can be clearly observed that January is much warmer over the Himalayas than December and February during wet seasons. This anomalous warming during January may be due to the presence of anomalous anticyclonic circulation, which in the process reduces flux exchanges from northern winter currents. This anomalous warming during January may contribute to a weakening of cyclonic formation in the sub-seasonal phase. At the mid-tropospheric level (data not shown), January also exhibits an anomalous warming over the Himalayan region, greater than that during December and February. Similarly, in the lower troposphere, at 850 hPa (data not shown), significant cooling occurs over the head of the Arabian Sea and the entire Indian subcontinent during December and February, in contrast to the relative warming observed during January.

To analyse the associated convection on the global scale, Fig. 4.9 illustrates the anomalous OLR for wet-minus-dry-month composites. The resulting OLR distribution shows a negative OLR (strong convection) over the eastern equatorial Pacific Ocean, a positive OLR (weak convection) over the western equatorial Pacific Ocean, and a negative OLR (strong convection) over the Indian Ocean. This distribution of OLR is related to warming (cooling) of the eastern (western) equatorial Pacific Ocean linked with El Niño. During the positive phase of El Niño, enhanced warming is associated with strong convection and hence enhanced cloud cover over the eastern equatorial Pacific region, whereas suppressed convection occurs over the western equatorial Pacific region due to anomalous cooling. This suppressed convection over the western equatorial Pacific Ocean generates increased anomalous cyclonic circulation over the Himalayan region due to the Rossby response (Kawamura 1998; Dimri 2013a). Convection associated with attenuated Walker circulation over the eastern equatorial Pacific Ocean remains similar during all 3 months, but convection is suppressed over the western equatorial Pacific Ocean, and convection over the equatorial Indian Ocean weakens more during January than during December and February. The Indian Ocean exhibits higher convection during December and February, which does not occur during January. The increased convection over the Indian Ocean is mainly suppressed by low-level clouds during the IWM (Bony et al. 2000). This stronger heating during December and February compared with January (around $\sim 60\text{--}70^\circ\text{E}$) enhances the Hadley circulation during December and February compared to January (Tanaka et al. 2004), along with an attenuated Walker circulation (Kawamura 1998). This increased Hadley circulation provides a greater mass transport from the Southern to Northern Hemisphere during December and February when compared to January.

Corresponding monthly moisture fluxes (wet–dry) and divergence were analysed to establish the repercussion of the dynamics discussed above. It depicts the enhanced convergence over the WH associated with the IWM during December, which almost becomes neutral during January and then shows higher convergence

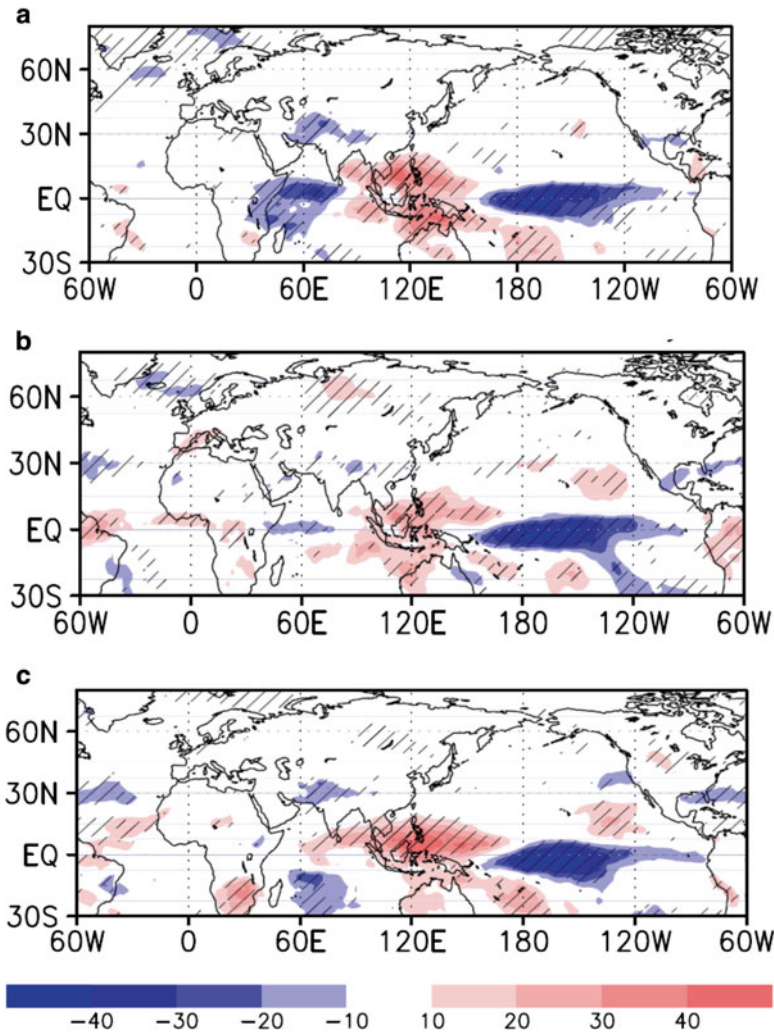


Fig. 4.9 Same as Fig. 4.8, but for outgoing longwave radiation (W/m^2 ; *shaded*)

during February. Stronger anomalous southwesterly moisture fluxes transport moisture from the equatorial Indian Ocean to the Himalayan region (Dimri 2007). During January, this flow weakens and becomes anomalously high over the Arabian Sea. To investigate this further, Fig. 4.10 illustrates the longitudinal–vertical cross-sectional distribution of anomalous meridional transport at $30^\circ N$ during wet (Fig. 4.10a, b, and c) and dry (Fig. 4.10d, e, and f) months. It can be clearly seen that wet conditions in December and February result in higher meridional moisture flux, which weakens during January particularly beyond $75^\circ E$ and in the lower troposphere. During dry composites, the opposite is seen.

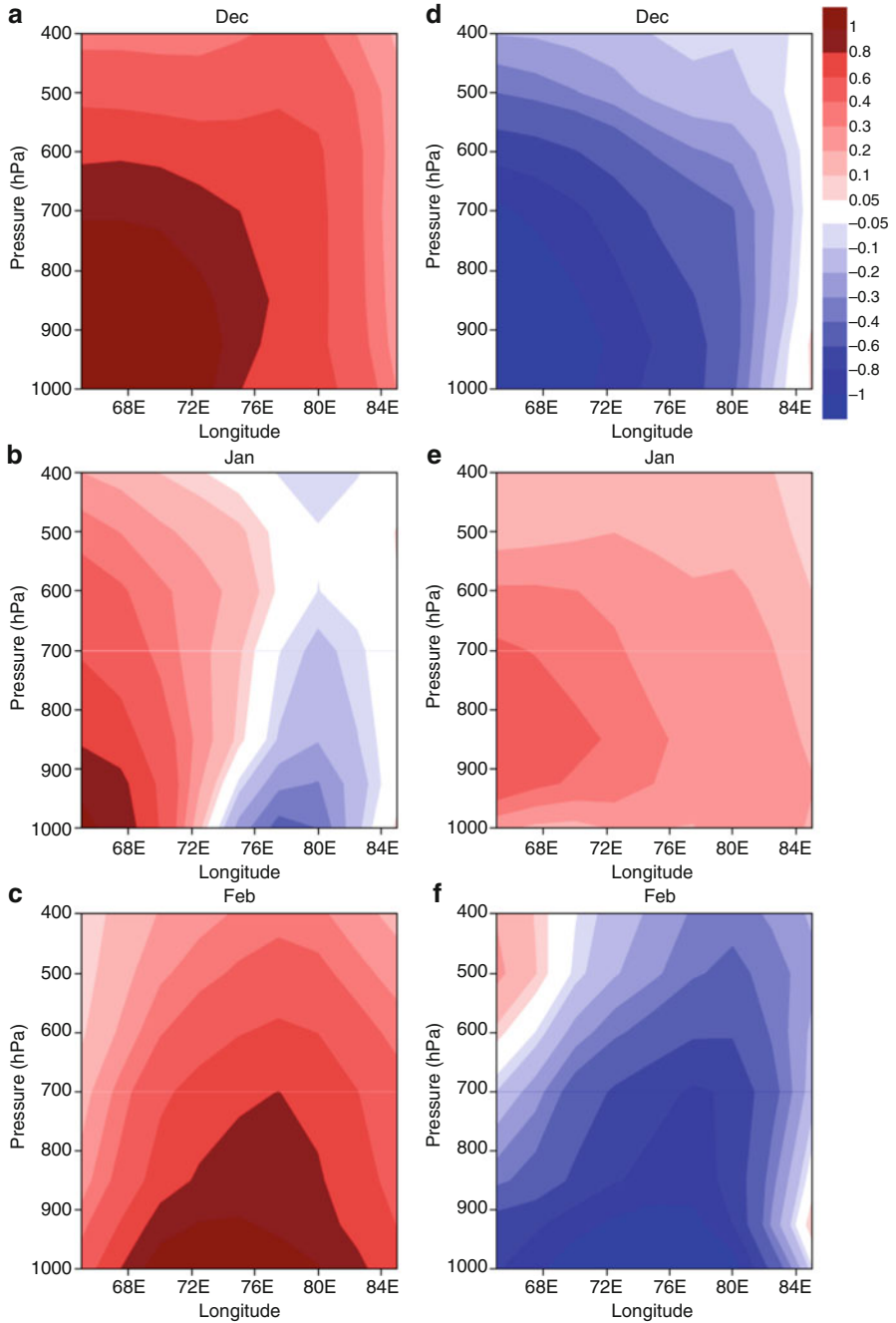


Fig. 4.10 Longitude–pressure vertical cross section at 30°N of the anomalous meridional moisture flux (kg/m/s) during wet ((a), (b), and (c)) and dry ((d), (e), and (f)) composites of Dec, Jan, and Feb, respectively

During an El-Niño phase, symmetric circulations over the equatorial Pacific Ocean, anticyclonic in the Northern Hemisphere and cyclonic in the Southern Hemisphere start building up in December and peak in February. The response from the IWM is similar throughout the winter. For the whole winter season (DJF), the IWM remains in phase with these when compared to January. The anomalous lower precipitation during January is influenced by sub-seasonal oscillations within the IWM. The discussion above suggests that warming/cooling of the Indian Ocean basin seems to be the dominant effect in defining sub-seasonal behavior during the IWM.

4.3.2 Large-Scale Global and Local Forcings

To determine large-scale global forcing, first the correlation of monthly winter precipitation over the WH with the concurrent and preceding months' sea-surface temperature (data not shown) for 28 years (1980–2007) was studied. The correlation of December and February monthly winter precipitation over the WH with the concurrent month's sea-surface temperature reveals similar patterns. Both were positively (negatively) correlated with the eastern (western) equatorial Pacific Ocean and the equatorial Indian Ocean sea-surface temperatures. This suggests that the eastern (western) equatorial Pacific Ocean warming (cooling) during December and February is in phase with the increased precipitation over the WH. For January, no significant correlation exists. Rather January precipitation is negatively correlated with the equatorial Indian Ocean sea-surface temperature for the preceding December, whereas February precipitation is strongly and positively correlated with equatorial Indian and western equatorial Pacific Ocean sea-surface temperatures for December and January. These results suggest that warming (cooling) over the eastern (western) equatorial Pacific Ocean influences December and February precipitation more than January precipitation. The Indian Ocean warming also influences December and February precipitation opposite to the influence found in January. A similar analysis using 2 m surface-air temperatures shows that January precipitation is influenced more by the preceding December surface-air temperature (data not shown). A correlation between January precipitation and December 2 m-surface temperature indicates that the preceding month's cooling over the equatorial Indian Ocean and the warming west of the WH provides conditions conducive to higher precipitation. December cooling over the north equatorial Pacific Ocean also corresponds to higher precipitation. A similar analysis using February precipitation and January temperature data produced opposite correlations. In this case, the equatorial Indian Ocean warming and the western (eastern) equatorial Pacific Ocean cooling (warming) were positively and strongly correlated. This may be attributed to the fact that, during the wet phase, January precipitation is controlled more strongly by the Indian Ocean temperature patterns, by local forcing over the WH region, or by both, and contrasts with conditions during December and February.

To further investigate the role of air temperature in controlling precipitation, anomalous air temperatures averaged over the WH region in wet and dry monthly composites are presented in Fig. 4.11a, b, respectively. During the wet phase, December and February temperatures show cooling (warming) in the middle (upper) troposphere. This is in contrast to January, when warming (cooling) takes place in the middle (upper) troposphere. January remains warmer (colder) in the middle (upper) troposphere than in December and February. Also, almost similar vertical temperature distributions from the surface to the mid-troposphere are seen during January. In the case of dry years, December and February remain warmer (colder) than January from the middle to upper (lower) troposphere. In wet and dry phases, both December and February show similar vertical distributions of air temperature compared with January. Such a distribution leads to the warmer mid-atmosphere during January. The WH area-averaged anomalous 2 m surface-air temperatures and anomalous precipitation for wet and dry years are shown in Fig. 4.11c, d. These data show that if the preceding month's surface temperature increases (decreases),

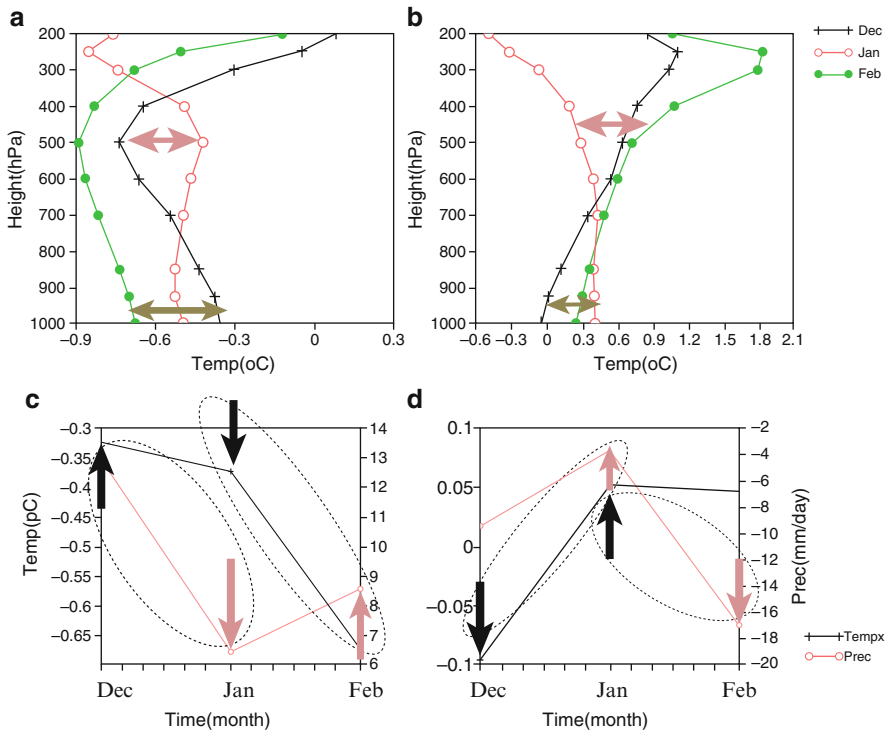


Fig. 4.11 Area-averaged (30°N 72°E to 37°N 82°E) vertical cross-sectional distribution of anomalous air temperature (°C) in (a) wet and (b) dry composites for Dec (black line), Jan (red line), and Feb (green line) and area-averaged (30°N 72°E to 37°N 82°E) anomalous 2-m surface-air temperature (black line; °C) and anomalous precipitation (mm/day) during (c) wet and (d) dry year composites of Dec, Jan, and Feb

the succeeding month's precipitation decreases (increases). Based on such an observation, a hypothesis is proposed that the preceding month's surface forcing also affects the succeeding month's precipitation. This hypothesis still needs to be studied in detail; however it is clear that sub-seasonal oscillations are observed in the IWM.

4.4 Intraseasonal Oscillation Associated with the Indian Winter Monsoon

Here robust features of the ISOs of the IWM and associated atmospheric circulation patterns are discussed. 28 years The WH daily precipitation (hereafter WHDP) (see bar), corresponding pentad climatology (see black curve with open circles) and 7–25-day filtered precipitation (see red curve with open circles) are shown in Fig. 4.12a. The ISO on sub-monthly timescales with active and break peaks is seen. Defined active (break) peak phases are considered which exceeded above (below) the 28-winter climatological 0.5 standard deviation in the 7–25-day WHDP anomalies. On doing so, 140 active and 119 break peak phases are identified. To investigate the temporal relationship of WHDP variability, circulation fields, OLR composites and daily time-lag composites were used.

Using the fast Fourier transform (FFT), the dominant mode of the ISO in the WHDP during the 28 winters was seen. WHDP (the first three harmonics of the annual cycle were removed) is detrended and masked from 15 November to 15 March (120 days) (Dimri 2013a, b). Figure 4.12b, c shows the FFT spectrum for the WHDP for 28 winters. A pronounced periodic ~16-day peak with a 95 % statistical significance appears (Fig. 4.12b). The corresponding Fig. 4.12c presents 28 years' power spectrum of IAV of the WHDP showing approximately a 16-day period scale in each year. This corresponds closely with the ensemble spectrum (Fig. 4.12b) at a sub-monthly-scale. Hence analysis of ISO mode of ~7–25 days-periodicity in the WHDP is proposed.

The sub-monthly scale pace-time structure of atmospheric circulation and convection in composites of active and break phases is investigated. Total 140 active- and 119 break-peak phases are chosen out of 28 years of climatology. A daily-lag composite of vertically integrated moisture flux and divergence from day –8 to day +8, based on the 7–25-day precipitation variation over the WH, is presented in Fig. 4.13. Day 0 corresponds to active precipitation-peak phases and day –8 and day +8 corresponds to break-peak phases. This cycle corresponds to a composite variation of 16 days. A peak-break phase is characterized by divergence over the WH with moisture exiting out of the region. On day –6, convergence builds up over the Arabian Sea near the Gujarat coast with fluxes still exiting out from the WH. On subsequent day –4, subtle changes in flux direction with shift in convergence zone towards the Himalayas is observed. Crucial flow transfer starts by this time with two breakaway streams. First one flows into the WH as the second move farther out

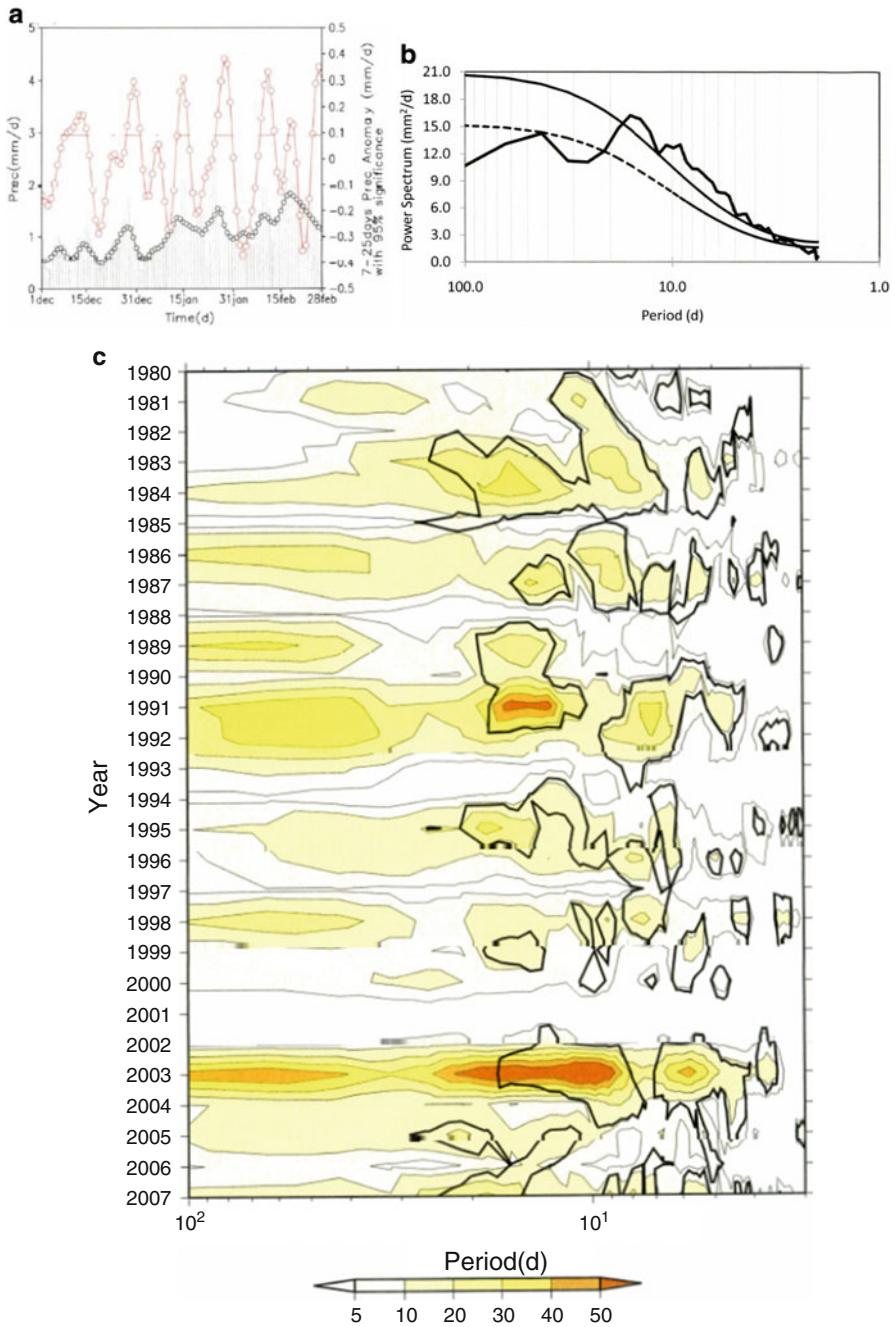


Fig. 4.12 (a) Based on 28 years (Dec 1979, Jan, Feb 1980 to Dec 2006, Jan, Feb 2007) of data, time-series of WHDP climatology (*bar; left axis*), pentad precipitation climatology (*black line with open circles; left axis*), and 7–25-day filtered precipitation anomaly (*red line with open circles; right axis*). The line of 95 % significance is also shown and the period above this corresponds to climatological active phases. (b) The 28-winter (DJF) ensemble spectrum of the WHDP time series from 15 Nov. to 15 Mar. (120 days). A red noise spectrum (*dashed curve*) and its 95 % level of significance (*solid curve*) are also shown. (c) Interannual variation in the WHDP spectrum from 1980–2007. The thick *black solid line* shows the 95 % level of significance

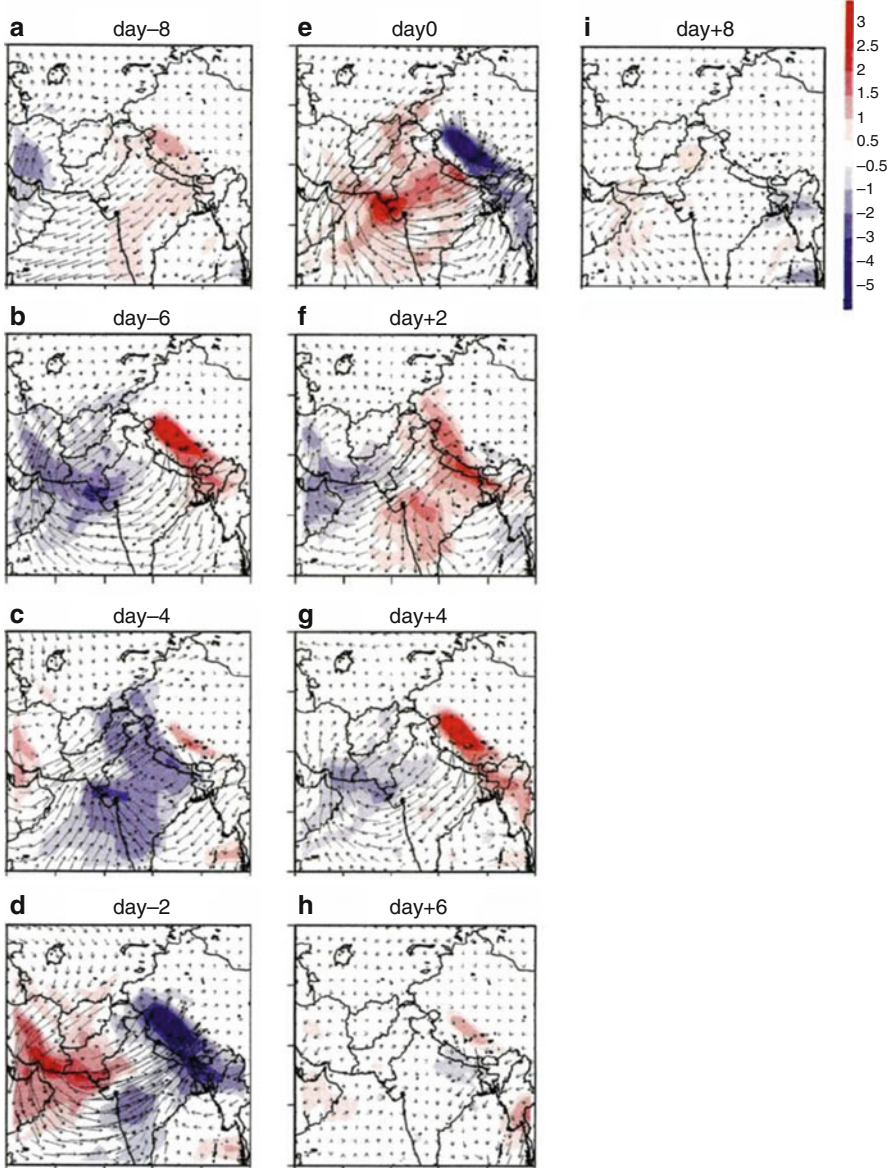


Fig. 4.13 Composite of vertical integrated moisture flux (vector; 40 kg/m/s) and divergence (*shaded*; $\times 10^5/s$) based on 7–25-day filtered values of specific humidity and wind anomalous fields from day –8 to day +8 based on WHDP. Day 0 corresponds to the active peak of 7–25-day WHDP variation. Values above 95 % statistically significant are plotted with *shade*

from the eastern Himalayas. During the precipitation peak in the active phase, well-defined moisture influx with a well-defined convergence zone over the Himalayas sets in. This characteristic weakens on day +2 with increased outflow and divergence over the Himalayas. Such a situation dominates and strengthens in the following days.

Daily-lag composites of 500 hPa stream function and wind from day -8 to day +8 based for 7–25-day precipitation variation over the WH are investigated to establish the character of dynamical atmosphere (Fig. 4.14). An anomalous higher stream function, corresponding to anticyclonic circulation, builds up over the western part of the WH on day -8. This moves eastwards on subsequent days. With this, on day -4, anomalous cyclonic circulation characterized by lower stream-function values develops over Saudi Arabia. Significant winds succeeding (preceding) the anomalous anticyclonic (cyclonic) circulation are seen. This situation of anomalous cyclonic circulation intensified and moved eastward over the Afghanistan and Pakistan region by day -2. Such a situation is as well associated with strong winds. On peak phase, day 0, intense wind located over the WH and adjoining Pakistan region dominate. It is interesting to note that the center of anomalous cyclonic circulation over and near the WH persists for at least 4 days, from day -2 to day +2. Such positioning provides a situation conducive to southwesterly moisture influx from the Arabian Sea during active peak phases. This dominance in association with the WDs' life cycle defines the rationale for higher precipitation in active phases. The Himalayan topography as well weakens, stagnates and/or changes the direction of the southwesterly flow and the significant winds. In the upper troposphere (200 hPa – data not shown), similar structure of the mid-troposphere dominates except that, at this level, a larger and more elongated significant area with significant southwesterly winds preceding the system persists. This vertical distribution of deep cyclonic circulation extends from the mid- to upper-troposphere during the peak active phase. The cascading of anomalous anticyclones and anomalous cyclones persist in the upper troposphere which on subsequent days decay and so on. The upper tropospheric anomalous cyclonic circulation persists longer than that found in the mid-troposphere.

Further OLR distribution from day -8 to day +8 based on the 7–25-day precipitation along with a similar distribution of 500 hPa stream-function and wind as shown in Fig. 4.14 (for better assessment) is illustrated in Fig. 4.15. Increased and faster advancement of the anomalous cyclonic circulation due to suppressed convection dominates over the Himalayan region. This deepens by day -4 and further build up of convection leads to more localized precipitation over the WH. Increased (suppressed) convection ahead (rear) of the anomalous cyclonic circulation is seen. The active peak displays strongest convection ahead of anomalous cyclonic circulation on day 0. Here as well, such a situation is seen occurring in a cascading manner which corresponds to a chain of anomalous cyclonic circulations, followed by another anomalous anticyclonic circulation, and so on.

To understand the periodic occurrences of alternating anomalous anticyclonic and cyclonic circulations and its association with associated precipitation, Fig. 4.16 presents time-lag composites based on 7–25-day active peak phases. It shows evolution

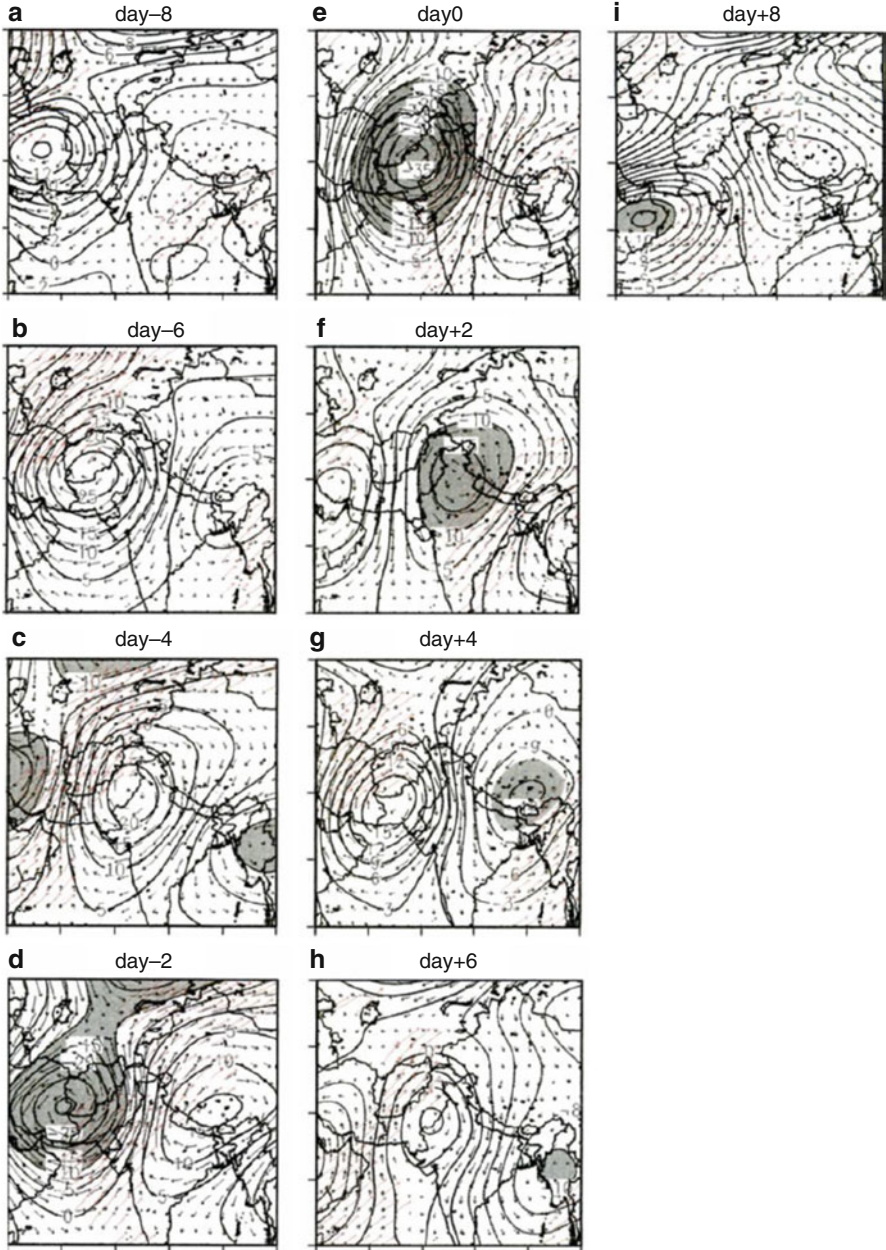


Fig. 4.14 Composite of 7–25-day filtered 500 hPa streamfunction ($\times 10^{-6} \text{ m}^2/\text{s}$) and wind (m/s) anomalies from day –8 to day +8 based on WHDP. Day 0 corresponds to the active peak of 7–25-day WHDP variation. The contour interval for streamfunction is $5 \times 10^{-6} \text{ m}^2/\text{s}$, and the 95 % statistically significant streamfunction is shaded. The strength of the wind vector is 15 m/s, and the 95 % statistically significant wind is plotted with red color

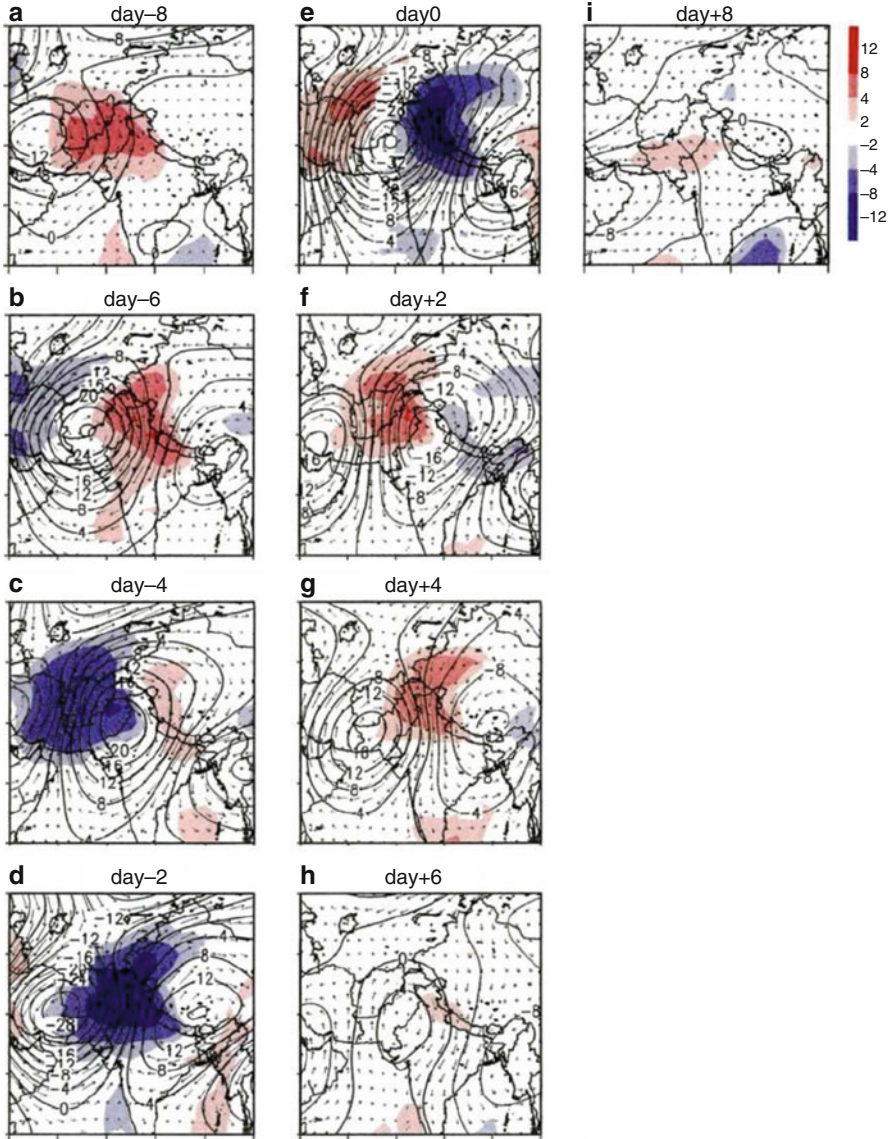


Fig. 4.15 Composite of 7–25-day filtered OLR (W/m^2 ; *shade*), 500 hPa streamfunction ($\times 10^{-6} m^2/s$), and wind (m/s) anomalies from day -8 to day $+8$ based on WHDP. Day 0 corresponds to the active peak of 7–25-day WHDP variation. The contour interval for streamfunction is $4 \times 10^{-6} m^2/s$. The strength of the wind vector is 5 m/s

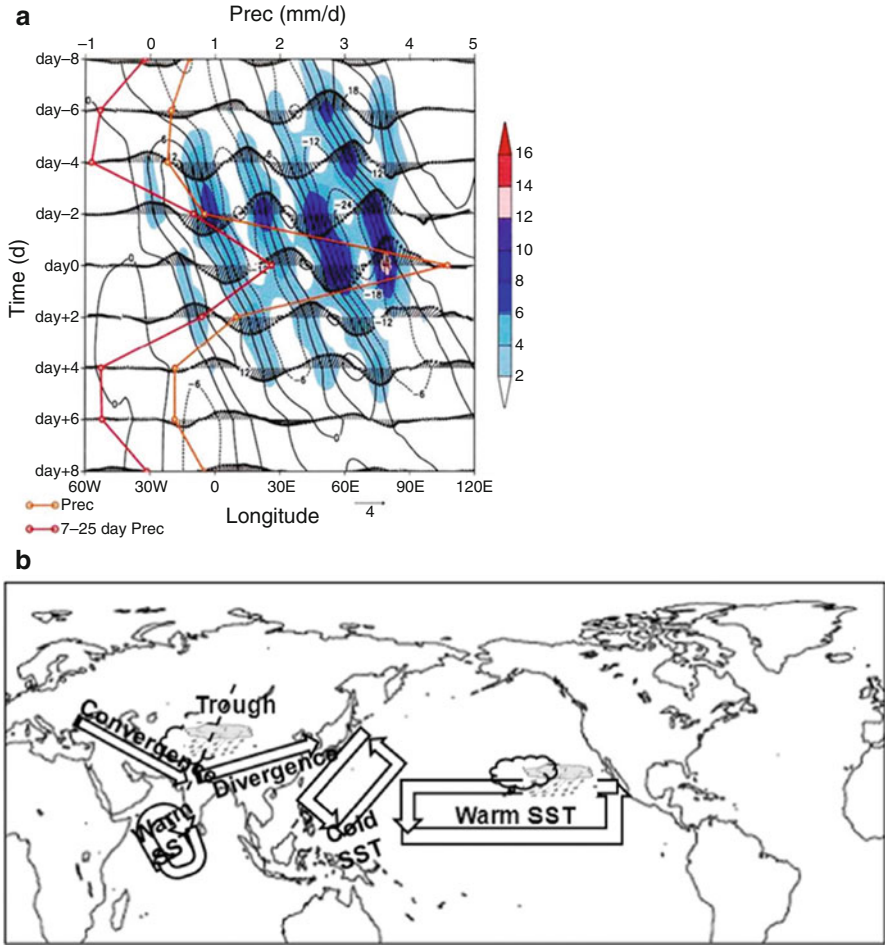


Fig. 4.16 Time-longitude cross-sectional distribution at 35°N of composites for 7–25-day filtered OLR (W/m^2 ; shade), 500 hPa height (hPa; contour), 500 hPa wind (m/s; arrow), and precipitation (mm/d; red curve; upper axis) anomalies from day –8 to day +8 based on WHDP. Day 0 corresponds to the active peak of 7–25-day WHDP variation. The yellow curve corresponds to anomalous precipitation (mm/d; yellow curve; upper axis) from day –8 to day +8 based on WHDP and (b) Schematic representation of physical mechanism associated with enhanced IWM during ENSO phases

of cyclonic systems which is in correspondence with the life cycle of the WDs. This conformity of WDs as a “family,” with one following the other in a symmetric wave which peaks at day 0, followed by subsequent decay, is associated with its precipitation distribution as well. Associated convection and corresponding 500 hPa height indicate the evolution of the storm by day –6 and/or day –4 with peaking by day 0. Wind distribution shows symmetrical in phase movement associated with each peaking cyclonic storm. Primarily WDs moves as a ‘family’ – a set of a number of evolu-

ing and decaying WDs - in periodic occurrences of alternating anomalous anticyclonic and cyclonic circulations. Such a traveling pattern forms a kind of wave structure. Figure 4.16a shows time-travel composites based on 28 years of data (1980–2008) for active WD peak phases. Here a very clear evolution of WD with time is seen. 'Family' structure – evolution and decay – in a phased manner in which one WD following the other in a symmetric wave followed by decay is seen. Such evolution associated with an outgoing long-wave corresponding to convection starts building up by day –6 and peaked on day 0. At 500 hPa, corresponding anomalous geopotential height depicts WD intensification starts by day –6 and/or day –4 which peak by day 0. Here as well, we see symmetrical phase movement associated with each WD at 500 hPa wind. Every WD peaked in a similar phase of wind. Associated precipitation is highest on day 0, and this shows the corroborative correspondence of its distribution as per the WD evolution and decay. This baroclinic structure is a dominant mechanism for storm intensification during storms evolution (Dimri 2013b).

To analyse the significant coupling with the SWJ during winter conditions and explicitly during enhance ENSO, warming over equatorial central/eastern Pacific and Indian Ocean provides attenuated Walker circulation. This warm episode over equatorial Pacific corresponding to the attenuated Walker circulation creates conditions for the SWJ to move southwards (Kawamura 1998; Dimri 2013a, b). In addition, significant cooling with an extension over eastern Pacific Ocean provides north–south gradient (Webster et al. 1998) provide a physical mechanism for an intense IWM over the WH (Fig. 4.16b). Such response produces anomalous WD evolution in the west of the WH. This significant cooling and convective heating over the equator results in the Rossby type of response. These two processes of increased convection over tropical Indian Ocean and anomalous WDs establish a strengthening Hadley circulation. In such provisioning, large scale meridional transport due to ascending atmospheric motion over the tropical Indian Ocean and descending motion over the west of Himalayan region become established. This coupling provides more moisture intake from the southern latitudes and which substantially adds moisture to the anomalous WDs and hence increases associated precipitation. Thus vertical baroclinic response over the Himalayan region provides more suitable condition for genesis/intensification of cyclonic storms (Fig. 4.16a) during wet conditions (Kawamura 1998). Therefore, such baroclinic response assists intensification of WDs and hence increases associated precipitation during wet years. This physical mechanism as well shows significant southward shifting of the SWJ over south Asian regions associated with deepening of northwesterly flow immediately west of northern India. Such situations are conducive to enhanced cold surges. As discussed, attenuated Walker circulation associated with El-Niño conditions and strengthened Hadley circulation due to asymmetric meridional upper tropospheric flow from the Southern Hemisphere to the Northern Hemisphere with strengthening of Hadley circulation work in tandem to push the SWJ southwards and help in providing moisture to evolved WDs. Such stationary wave-phase formation in the mid-troposphere provides suitable conditions for genesis/intensification of WDs/troughs. Also, vertical structure from the lower to the upper troposphere strengthens the formation of such synoptic weather resulting in higher precipitation over the WH.

A physical mechanism of interannual variability associated with the IWM during wet years shows significant southward shift of the SWJ over south Asian regions. It manifests in a deepening of the northwesterly incoming flow over the northern Indian region. This situation is favorable for enhanced cold surges associated with WDs. Increased convection over the central equatorial Pacific region corresponds to higher convection and hence attenuated Walker circulation. In tandem with it, a strengthened Hadley Cell causing asymmetric meridional upper tropospheric flow from the Southern to Northern Hemisphere forms a stationary wave in the mid-troposphere. This situation supports genesis/intensification of WDs/troughs consisting of more frontal systems. Such a situation corresponds to higher precipitation over the WH. Although the interannual variability of individual months is in phase with seasonal interannual variability, the interannual variability of individual months is not in phase with other months. A positive ENSO phase corresponds to a southward positioning/shifting of the 200 hPa SWJ. The reduction in January precipitation is influenced by the equatorial Indian-Ocean surface temperature due to the weakening of the Hadley response during January compared to December and/or February. Additionally, comparatively greater middle-tropospheric warming during January enhances the middle tropospheric anticyclone with an increased northerly wind to the east compared to December and February. Such sub-seasonal/bimonthly oscillations in the IWM correspond to higher precipitation during December and February relative to January. ISO characteristics associated with the WHDP show an average life cycle of approximately 10–12 days of evolution and decay. Dominance of ~16-day periodicity is associated with the WHDP. Correspondingly, a cascading wave train of peaking and decaying of cyclonic storm is observed. In the active peak phase, convective activities in association with westerly to southwesterly enhanced moisture flux dominates and provides higher precipitation. Convection in association with the storm seems to always precede anomalous cyclonic circulation. A succession of cyclonic–anticyclonic–cyclonic, and so on, circulation dominates in the SWJ.

References

- Adler RF, Huffman GJ, Chang A, Ferraro R, Xie P, Januaryowiak J, Rudolf B, Schneider U, Curtis S, Bolvin J, Gruber A, Susskind J, Arkin P (2003) The version 2 global precipitation climatology project (GPCP) monthly precipitation analysis (1979–present). *J Hydrometeorol* 4:1147–1167
- Annamalai H, Hamilton K, Sperber KR (2007) The south Asian summer monsoon and its relationship with ENSO in IPCC AR4 simulations. *J Clim* 20:1071–1092
- Bony S, Collins WD, Fillmore DW (2000) Indian ocean low clouds during the winter monsoon. *J Clim* 13:2028–2043
- Dai J (1990) Climate in the Qinghai-Xizang Plateau (in Chinese). China Meteorol Press, Beijing
- Das S, Singh SV, Rajagopal EN, Gall R (2003) Mesoscale modeling for mountain weather forecasting over the Himalayas. *Bull Am Meteorol Soc* 84:1237–1244
- Dimri AP (2004) Impact of horizontal model resolution and orography on the simulation of a western disturbance and its associated precipitation. *Meteorol Appl* 11:115–127

- Dimri AP (2006) Surface and upper air fields during extreme winter precipitation over the western Himalayas. *Pure Appl Geophys* 163:1679–1698
- Dimri AP (2007) The transport of momentum, sensible heat, potential energy and moisture over the western Himalayas during the winter season. *Theor Appl Climatol* 90(1–2):49–63
- Dimri AP (2012) Relationship between ENSO phases with northwest India winter precipitation. *Int J Climatol* 33(8):1917–1923. doi:[10.1002/joc.3559](https://doi.org/10.1002/joc.3559)
- Dimri AP (2013a) Interannual variability of Indian winter monsoon over the western Himalaya. *Glob Planet Chang* 106:39–50
- Dimri AP (2013b) Intraseasonal oscillation associated with the Indian winter monsoon. *J Geophys Res* 118:1–10
- Dimri AP (2014) Sub-seasonal interannual variability associated with the excess and deficit Indian winter monsoon over the western Himalayas. *Clim Dyn* 42(7–8):1793–1805
- Dimri AP, Mohanty UC (2009) Simulation of mesoscale features associated with intense western disturbances over western Himalayas. *Meteorol Appl* 16:289–308
- Dimri AP, Niyogi D (2012) Regional climate model application at subgrid scale on Indian winter monsoon over the western Himalayas. *Int J Climatol* 33(9):2185–2205
- Dimri AP, Yasunari T, Wiltshire A, Kumar P, Mathison C, Ridley J, Jacob D (2013) Application of regional climate models to the Indian winter monsoon over the western Himalayas. *Sci Total Environ*. <http://dx.doi.org/10.1016/j.scitotenv.2013.01.040>
- Duchon CE (1979) Lanczos filtering in one and two dimensions. *J Appl Meteorol* 18:1016–1022
- Goswami BN, Mohan RSA (2001) Intraseasonal oscillations and interannual variability of the Indian summer monsoon. *J Clim* 14:1180–1198
- Hadley Centre (2006) HadiSST 1.1 global sea-ice coverage and SST (1870-present). British atmospheric Data Centre. <http://badc.nerc.ac.uk/data/hadisst>
- Hartmann DL, Michelsen ML (1989) Intraseasonal periodicities in Indian rainfall. *J Atmos Sci* 46:2838–2862
- Hoyos CD, Webster PJ (2007) The role of intraseasonal variability in the nature of Asian monsoon precipitation. *J Clim* 20:4402–4424
- Kanamitsu M, Ebisuzaki W, Woollen J, Yang S–K, Hnilo JJ, Fiorino M, Potter GL (2002) NCEP–DEO AMIP-II reanalysis (R-2). *Bull Am Meteorol Soc* 83(11):1631–1643
- Kawamura R (1998) A possible mechanism of the Asian summer monsoon–ENSO coupling. *J Meteorol Soc Jpn* 76:1009–1027
- Kripalani RH, Kumar P (2004) Northeast monsoon rainfall variability over south peninsular India vis-à-vis Indian ocean dipole mode. *Int J Climatol* 24:1267–1282
- KrishnaKumar K, Rajagopalan B, Cane MA (1999) On the weakening relationship between the Indian monsoon and ENSO. *Science* 284(5423):2156–2159
- KrishnaKumar K, Rajagopalan B, Hoerling M, Bates G, Cane MA (2006) Unraveling the mystery of Indian monsoon failure during El Niño. *Science* 314(5796):115–119
- Kumar P, Rupakumar K, Rajeevan M, Sahai AK (2007) On the recent strengthening of the relationship between ENSO and northeast monsoon rainfall over South Asia. *Clim Dyn* 28:649–660
- Laat ATJ, Lelieveld J (2002) Interannual variability of the Indian winter monsoon circulation and consequences for pollution levels. *J Geophys Res* 107(D24):4739. doi:[10.1029/2001JD001483](https://doi.org/10.1029/2001JD001483)
- Lang TJ, Barros AP (2004) Winter storms in central Himalayas. *J Meteorol Soc Jpn* 82(3):829–844
- Liebmann B, Smith CA (1996) Description of complete (interpolated) outgoing longwave radiation dataset. *Bull Am Meteorol Soc* 77:1275–1277
- Mitas CM, Clement A (2005) Has the Hadley cell been strengthening in recent decades? *Geophys Res Lett* 32. doi:[10.1029/2004GL021765](https://doi.org/10.1029/2004GL021765)
- New MG, Hulme M, Jones PD (2000) Representing twentieth century space time climate variability, part II: development of a 1901–96 monthly grids of terrestrial surface climate. *J Clim* 13:2217–2238
- Oort AH, Yienger JJ (1996) Observed interannual variability in the Hadley circulation and its connection to ENSO. *J Clim* 9(11):2751–2767

- Raman CRV, Maliekal JA (1985) A northern oscillation relating northern hemispheric pressure anomalies and the Indian summer monsoon? *Nature* 314:430–432
- Rudolf B, Beck C, Grieser J, Schneider U (2005) Global precipitation analysis products. Global Precipitation Climatology Centre (GPCC), DWD, Internet publication, pp 1–8
- Saha SK, Halder S, KrishnaKumar K, Goswami BN (2011) Pre-onset land surface processes and ‘internal’ interannual variabilities of the Indian summer monsoon. *Clim Dyn* 36:2077–2089
- Sato T, Kimura F (2007) How does Tibetan Plateau affect transition of Indian monsoon rainfall? *Mon Weather Rev* 135:2006–2015
- Tanaka HL, Ishizaki N, Kitoh A (2004) Trend and interannual variability of Walker, monsoon and Hadley circulations defined by velocity potential in the upper troposphere. *Tellus* 56A:250–269
- Turner AG, Inness PM, Slingo JM (2007) The effect of double CO₂ and model basic state biases on the monsoon ENSO system. I: mean response and interannual variability. *Q J Roy Meteorol Soc* 133:1143–1157
- Webster PJ, Magana VO, Palmer TN, Shukla J, Tomas RA, Yanai M, Yasunari T (1998) Monsoons: processes, predictability, and the prospects for prediction. *J Geophys Res* 103:14451–14510
- Wu TW, Qian ZA (2003) The relation between the Tibetan winter snow and the Asian summer monsoon and rainfall: an observational investigation. *J Clim* 16(12):2038–2051
- Yadav RK (2012) Why is ENSO influencing India north-east monsoon in the recent decades? *Int J Climatol* 32(14):2163–2180. doi:[10.1002/joc.2430](https://doi.org/10.1002/joc.2430)
- Yadav RK, Yoo JH, Kucharski F, Abid MA (2010) Why is ENSO influencing northwest India winter precipitation in recent decades? *J Clim* 23:1979–1993. doi:[10.1175/2009JCLI3202.1](https://doi.org/10.1175/2009JCLI3202.1)
- Yadav RK, Ramu DA, Dimri AP (2013) On the relationship between ENSO patterns and winter precipitation over North and Central India. *Global Planet Change* 107:50–58. doi:[10.1016/j.gloplacha.2013.04.006](https://doi.org/10.1016/j.gloplacha.2013.04.006)
- Yasunari T, Kitoh A, Tokioka T (1991) Local and remote responses to excessive snow mass over Eurasia appearing in the northern spring and summer climate. *J Meteorol Soc Jpn* 69:473–487
- Yatagai A, Kamiguchi K, Arakawa O, Hamada A, Yasutomi N, Kitoh A (2012) APHRODITE: constructing a long term daily gridded precipitation dataset for Asia based on a dense network of rain gauges. *Bull Am Meteorol Soc*. doi:[10.1175/BAMS-D-11-00122.1](https://doi.org/10.1175/BAMS-D-11-00122.1)